EES Batteries

Accepted Manuscript

This article can be cited before page numbers have been issued, to do this please use: C. Renais, M. Mirolo, V. Vanpeene, M. Servajon, J. Drnec, F. Alloin and C. Villevieille, *EES Batteries*, 2026, DOI: 10.1039/D6EB00003G.

View Article Online
DOI: 10.1039/D6EB00003G

Fast-charging lithium-ion batteries are essential for the widespread adoption of electric vehicles and the efficient use of renewable energy, yet their electrochemical performance remains limited by a fundamental trade-off between energy and power density. This limitation is particularly true for graphite negative electrodes, which, despite their commercial use, exhibit strong rate limitations that can lead to non-uniform lithiation, accelerated ageing, and safety risks under high-power operation.

While electrode engineering strategies such as calendering and porosity optimisation are commonly employed to improve power performance, their impact on ion transport and reaction heterogeneity within working electrodes remains poorly understood. By combining electrochemical measurements, three-dimensional microstructural characterisation, and operando spatially resolved X-ray diffraction, this study directly links electrode microstructure to lithium-ion transport limitations and lithiation gradients in graphite electrodes.

The results demonstrate that increased tortuosity in low-porosity electrodes leads to severe ionic transport limitations, heterogeneous current distribution, and local effective C-rates significantly exceeding the applied current. These findings highlight the critical role of three-dimensional microstructure in governing fast-charging behaviour and emphasise the need for spatially resolved design principles to develop safer, longer-lasting, and high-power batteries for sustainable energy applications.

DOI: 10.1039/D6EB00003G

Understanding fast charging ability limitation in graphite electrode for Li-ion batteries.

Heterogeneities of lithiation in conventional electrodes.

Corentin Renais[a], Marta Mirolo[b], Victor Vanpeene[c], Maxime Servajon[a], Jakub Drnec[b], Fannie Alloin[a,*], Claire Villevieille[a,*]

a. *Univ. Grenoble Alpes, Univ. Savoie Mont Blanc, CNRS, Grenoble INP, LEPMI, Grenoble, France*

b. *ESRF, Experimental and Research Division, Grenoble, France*

c. *Université Grenoble Alpes, CEA, CNRS, IRIG, SyMMES, Grenoble, France*

Corresponding authors: fannie.alloin@grenoble-inp.fr; claire.villevieille@grenoble-inp.fr

Abstract

Graphite electrode dominates the Li-ion batteries market as a negative electrode material. As a consequence, it is of the utmost importance to understand the origin of its power limitation for fast charging applications in electric vehicles. We first investigated thick and porous graphite electrodes using rate capability tests by varying the electrode porosity and the salt concentration, showing a first correlation between porosity, salt concentration, and high-power capability. By using X-ray holo-tomography at large-scale facilities, we probed the microstructure of the electrodes showing the increase of tortuosity as function of the porosity. These gathered results were strengthened by using *operando* vertical profile high resolution X-ray diffraction. Heterogeneities of lithiation along the electrode thickness were found by varying the electrode porosity and the cycling rate from C/4 to C/1. The highest tortuosity results in large ionic transport hindrance along the electrode thickness. The in-depth investigation demonstrated that larger heterogeneities through the electrode thickness are observed. This heterogeneity depends on the graphite reaction mechanisms and are more pronounced in biphasic domain ascribed to flat potential plateau. Finally, by correlating all the results, we were able to estimate the local current densities and demonstrated that effective local C-rate can reach twice the applied C-rate, raising serious concerns about ageing phenomenon in batteries.

Introduction

Power and energy densities are key parameters to develop better energy storage systems[1]. Unfortunately, in conventional Li-ion batteries (LiBs), these properties are antagonists, which prevent long-range/fast charging in electric vehicles, as an example. Strategies need to be developed to address this issue or at least understand the limitation. Currently, electrode engineering is at the core of LiBs research to at least buffer this issue. Classical procedures consist of optimising the loading (control of electrode thickness and “travelling” distance of the charges), the electronic percolation (improving power density), and porosity (both ionic and electronic percolation) of electrodes to find an optimal ratio between energy and power for a given application. Unfortunately, graphite negative electrode is the most subject to this limitation, even with dedicated engineering. The underlying challenge is then to find the causes of this limitation and address those weaknesses.

View Article Online
DOI: 10.1039/D6EB00003G

To identify the process(es) that limit the power capability of the graphite electrodes, researchers investigated the impact of the electrode engineering, in particular, the electrode porosity, as it allows tuning of electronic and ionic transport. Generally, the optimal porosity is set between 30% and 50% [2, 3]. Antartis *et al.* concluded that the optimal porosity of the electrode is around 45%, when containing graphite whose particle size is below 20 µm [4]. Indeed, they did not observe any gain in specific capacity for porosities greater than 50%, since a similar and optimal wetting of the electrode was obtained above this value. However, in this case, the specific capacity fading was more pronounced and was related to a lack of mechanical strength at the electrode level, leading to progressive active material inactivity. For porosities smaller than 30%, the compacity of the electrode induces more stress on the particles during the lithiation process, due to the swelling of the particles themselves (around 13% expansion of the unit cell volume [5]) and it induces specific capacity loss along cycling. For porosities between 30 and 50%, the authors attributed the lower specific capacity obtained at a C/5 rate (porosity of 37%) compared to the one obtained at C/20 to a limited transport of lithium ions through the denser graphite microstructure, while this limitation was less pronounced at a porosity of 49%. Similar results were obtained on $LiFePO_4$ electrodes, as demonstrated by Fongy *et al.* An electronic limitation is observed in the case of low electrode compacity (high porosity), whereas an ionic one occurs for denser electrodes [6, 7].

A power limitation in an electrode could lead to lithiation heterogeneities in the electrode volume that could originate from ionic and/or electronic transport. Newman *et al*., employing a modelling approach, accounted for such heterogeneities in porous electrodes by introducing a penetration depth concept [8]. The concept of penetration depth, expressed in a dimensionless form, was later extended to incorporate other relevant parameters, such as salt concentration and transference number. Based on the work of Doyle *et al.* [9], Fuller *et al.* modelled the discharge behaviour of a graphite/MnO_2 cell and highlighted that the main process that limited power capability was the concentration gradient due to salt depletion [10]. More recently, Gallagher *et al.* further developed the model and discussed the effect of current density on penetration depth in $LiNi_{0.8}Co_{0.15}Al_{0.05}O_2$/graphite cells [11]. Tambio *et al.* using Gallagher's results demonstrated the importance of micrometric pores percolation in homogenisation of salt concentration in $LiNi_{0.5}Mn_{0.3}Co_{0.2}O_2$ electrode [12]. In all cases, the concept of penetration depth discusses the appearance of a salt concentration gradient along the electrode thickness that, in the worst case, could reach a concentration of zero. Dufour *et al.* investigated lithium concentration gradients as a function of the electrode loading and C-rate with simulations [13]. Using a spatial quantification of heterogeneity with the Normalised Absolute Average Deviation (NAAD) function, first introduced by Gu [14], heterogeneities in the composite electrode were observed in correlation with the formation of the intercalation stages IV, II and I, stages mainly driven by a biphasic mechanism of lithium storage. Inversely, smaller heterogeneities were observed for solid solution phase mechanisms.

Experimentally, these inhomogeneities were also investigated. A lithium inventory mapping of electrode (LIME) was developed combining both X-Ray diffraction (XRD) and X-ray fluorescence (XRF) to probe at the same time the structural state of charge and the electrolyte concentration[15]. Using imaging, *operando* optical microscopy experiments were performed[16]. Kang *et al.* observed a front of lithiation from the separator/electrode interface toward the electrode/current collector interface, demonstrating a power limitation coming from the electrolyte[17]. Unfortunately, quantitative estimation of the active material state of charge was not possible with this approach. X-ray diffraction, despite being a bulk technique with no visual evolution of lithium concentration gradient, could play a key role. Based on energy-dispersive XRD, Yao *et al.* quantified lithiation gradients in graphite electrode in a full cell graphite/NMC532. They observed that lithiation occurs first near the separator before propagating toward the current collector, demonstrating a limitation from the diffusion of lithium ions

View Article Online
DOI: 10.1039/D6EB00003G

through the electrolyte[18]. Tardif *et al.* used several literature data to report an average q scattering vector for region containing LiC_6 (001) and graphite (002) Bragg reflections in correlation with the state of charge of a graphite half-cell, establishing a pseudo-calibration curve to determine the graphite state of charge from a diffraction pattern [19]. The authors denoted a delithiation gradient from the separator toward the current collector and quantitatively estimated the heterogeneity in graphite delithiation with the NAAD function. Compared to the study by Dufour *et al.*, a similar evolution in the state of charge dispersion was observed for $x < 0.5$, but no dispersion was indicated for stage I formation ($x > 0.5$) which is inconsistent with the model results.

To date, there has been a lack of correlation between the lithiation heterogeneities in the electrode thickness and the electrode engineering parameters, in particular, the microstructure (porosity and tortuosity), but also with other engineering parameters such as the salt concentration. In this study, the microstructure of graphite electrode with two porosities was investigated by means of tomography measurement and correlated to rate capability measurement and *operando* XRD using vertical profiling along the electrode thickness. The correlation between the electrochemical data and the structural properties evidenced the effect of electrode's microstructure, in particular, in hindering Li-ion transport properties which as a consequence contributed to poor power capability of graphite electrodes.

Material and methods

Electrode preparation and coin cell assembly

A suspension mixture composed of 80%$_{wt}$ of SFG 6L graphite powder (Imerys), 10%$_{wt}$ of Super C65 black carbon (Imerys) and 10%$_{wt}$ of PVDF HSV900 (Arkema) in N-methyl-2-pyrrolidone (NMP, Sigma Aldrich) was prepared and spread onto a copper foil used as current collector of 10 µm thickness, using a Doctor blade with 600 µm blade height. The slurry was dried at 70°C overnight, and electrode disks of 12 mm diameter were cut. From this process, porosities of 70 ± 5% (~120 µm of thickness) and loading of 6 ± 0.5 mg.cm^{-2} are obtained. The reduction to 50% (75 – 80 µm) or 30% (50 – 55 µm) porosity was achieved using a calendaring machine (MTI, MSK-HRP-01). The calendaring process was performed at room temperature by applying a dedicated pressure, then the electrodes was compressed at least three times at each pressure with a speed set to value (7 on the apparatus).To remove residual water, electrodes were dried overnight in a Büchi system at 90°C under dynamic vacuum (10^{-3} bar), before being introduced into a glovebox. The electrodes were mounted on CR2032 coin cells in an Ar-filled glovebox with < 1 ppm O_2 and H_2O. Half cells were mounted incorporating the graphite electrode, a glass fibre separator (Whatman) filled with 150 µL of LP30 (1M $LiPF_6$ in EC/DMC 1:1%$_v$, Solvionic) and a 750 µm thick lithium metal disk of 12 mm diameter as counter electrode (S4R supplier). Each electrochemical cycling was reproduced with three cells to ensure the reliability of the measurement. A standard deviation was extracted on the specific capacity obtained as a function of the cycling rate. This standard deviation is included in the plots analyzing the rate capability.

Cycling conditions and rate capability tests

All half cells are preliminarily cycled in a thermoregulated chamber at 25°C (± 0.1°C), with two cycles at a C/20 cycling rate between 1.2 – 0.01 V, with the first cycle enabling proper formation of the solid electrolyte interphase (SEI). Then, the rate capability tests consist in increasing the C-rate from C/10 to 4C, with each cycling at specific rate repeated three times. The cycling protocol uses a classical constant current-constant voltage (CCCV) procedure with 30 min CV period, between 1.2 – 0.01 V. In the rest of the article, all potentials always refer to the reference redox couple Li^+/Li.

Tortuosity measurement

View Article Online
DOI: 10.1039/D6EB00003G

Symmetric cells made of graphite electrodes were mounted in coin cells (12 mm diameter) and a glass fibre separator filled with 100 µL of 0.35 M $LiPF_6$ in EC/DMC (1:1%$_v$). The graphite electrodes used are the same (SFG 6L) as for rate capability tests, and the porosity ranged from 70% (pristine) to 50% and 30% by calendaring. The coin cells were characterised by electrochemical impedance spectroscopy (EIS) at open circuit voltage (OCV), between 1 MHz and 1 Hz with a perturbation amplitude of 10 mV using a SP150 (Biologic) at 25°C (± 0.1°C). The impedance diagrams are recorded ten times every 30 minutes and the results are averaged. The measured impedance diagrams are fitted using a transmission line model (TLM) using RelaXis software as described by Landesfeind *et al.* [20] (**Note 1, Supporting Information**). The ionic conductivity of the electrolyte was assessed by using a dedicated conductivity cell.

X-ray holotomography measurements and data treatment

Graphite electrode disks of 50 % and 30% porosity were cut in thin lamella (few hundreds of micrometres in width) using a razor blade. The lamellas were glued to brass pins and placed in a sample holder made of PFA sealed under Ar thanks to a UV-curing glue. Acquisitions were performed at the ESRF ID16B beamline[21] using the holo-tomography technique[22]. Scans composed of 4 consecutive acquisitions at each distance were constituted of 2505 projections, as well as 20 and 21 reference and dark images respectively, that were recorded on a PCO edge 5.5 CMOS camera (2048×2048pixels^2) with a 17 µm thick LSO scintillator along a 360° rotation. For the incident X-ray beam, an energy of 29.45 keV and photon flux 3.4 10^{11} ph.s^{-1} were measured, hence an exposure time of 10 ms per projection. Acquisitions were performed at a voxel size of 50 nm, resulting in fields of view of 102×102 µm^2. 3D reconstructions were achieved in two steps: (i) phase retrieval calculation using an in-house developed octave script based on a Paganin-like approach using a delta/beta ratio of 2740, and (ii) filtered backprojection reconstruction using ESRF software PyHST2[23]. Final volumes of 102×102×102 µm^3 with a voxel size of 50 nm in a 32-bit floating point were obtained. Post-processing ring removal and 8-bit conversion was performed using a dedicated Matlab script[24]. Analyses were performed on the reconstructed 8-bit volumes using the ImageJ software[25]. The different phases were segmented using a machine learning based random forest classifier embedded within the Ilastik software[26]. Additional details on image analysis and tortuosity calculation are presented in **Note 2**, **Supporting Information**).

X-ray diffraction measurements and data treatment

X-ray diffraction experiments were performed at ESRF ID31 beamline. Coin cells were cycled at C/4, C/2 and C/1 rates using a SP150 potentiostat (Biologic) in a thermoregulated environment at 25°C (± 0.1°C). To ensure a reliable vertical profiling experiment, the coin cells were aligned parallel to the beam so that the X-rays travelled through the whole diameter of the graphite electrodes. For the electrode with 50% porosity, the electrode thickness (around 75 µm) was probed with steps of 16 µm over a thickness of 90 µm. In the end, five *z*-positions localised in the electrode thickness were analysed, each of them labelled in agreement with their relative position in the electrode thickness L (0.1 L, 0.3 L, 0.5 L, 0.7 L and 0.9 L; 0.1 L being near the separator and 0.9 L near the current collector). For the electrode with 30% porosity, the electrode thickness (around 50 µm) was probed with steps of 5 µm. Nine *z*-positions were analysed corresponding to relative positions from 0.1 L to 0.9 L, with steps of 0.1 L.

A Pilatus 2M CdTe 2D detector (Dectris) has been used for the acquisition of the diffracted signal, positioned roughly 1 m from the sample. The beam energy was set at 75 keV, and the beam was focused on the sample (approximately 5 µm x 15 µm, vertical x horizontal). The 2D images are integrated into 1D diffraction pattern using the pyFAI package [27].

View Article Online
DOI: 10.1039/D6EB00003G

Data treatment was performed using Python software with *Matplotlib* [28] and LMFIT [29] libraries. A baseline subtraction on the 1D diffraction patterns was realised using a SNIP (Statistics-sensitive Non-linear Iterative Peak-clipping) algorithm from PyBaseline library [30].

Results and discussion

a. Electrochemical characterisation

To assess power limitations, we investigated graphite electrodes with two different porosities, 50% and 30%, as a function of the applied cycling rate (rate capability tests [31, 32, 33]) and of the salt concentration in the electrolyte (1 M, 0.7 M and 0.35 M $LiPF_6$ in EC/DMC 1:1%$_v$). **Figure 1a** shows the evolution of the galvanostatic fraction (CC) over the total specific capacity obtained by CCCV depending on the applied C-rate, for 50% and 30% porosity graphite electrodes. The inset shows the specific galvanostatic capacities obtained for each cycle for both electrode porosities. At slow cycling rates (C/20 – C/6), stable specific galvanostatic capacities are obtained (slightly decreasing from 383 mAh.g^{-1} to 358 mAh.g^{-1}) for both electrode porosities. Note that the obtained specific capacities exceed the theoretical specific capacity of graphite because of additional charges coming from the adsorption of Li^+ on nano-particles of carbon additive, increasing the maximal specific capacity of the composite electrodes. A difference appears at C/4 rate, when a lower specific galvanostatic capacity is observed for the electrode with the 30% porosity, compared to the one at 50% porosity. Notably, at fast charging rates (above C/2), the electrode can no longer reach graphite's theoretical specific charge. By increasing the cycling rate to 2C, a larger difference is noticed in the achievable capacity, as a function of the electrode porosity. The highest difference is obtained at C/1.5, with a galvanostatic specific capacity of 230 mAh.g^{-1} for the electrode with 30% porosity, whereas 273 mAh.g^{-1} is achieved for the electrode with 50% porosity. For higher cycling rates (2C – 4C), a stabilisation of the specific galvanostatic capacities is observed, representing less than 20% of the total specific capacities for both porosities. At this stage, Li plating could play also a role but from an electrochemical perspective, monitoring lithium plating during lithiation remains challenging, while it becomes less so during delithiation as lithium is oxidized. Careful examination of our delithiation curves revealed no evidence of a plateau associated with Li plating, even at high charging rates. However, in this range and even at faster charging rate, we suspect that the lithium counter electrode takes the lead in terms of kinetic limitation, inducing a large counter electrode polarization. Lu et al. further investigated the failure mechanisms for fast charged Li metal batteries with liquid electrolyte[34]. They demonstrated that at rates higher than 1C rate, already Li can be detrimental for cycling. On top of the Li metal counter electrode limitation, the half-cell would many deliver "capacitive" charges since no capacity from intercalation could be achievable. This explains why the specific galvanostatic capacity reaches a plateau for high C-rates.

View Article Online
DOI: 10.1039/D6EB00003G

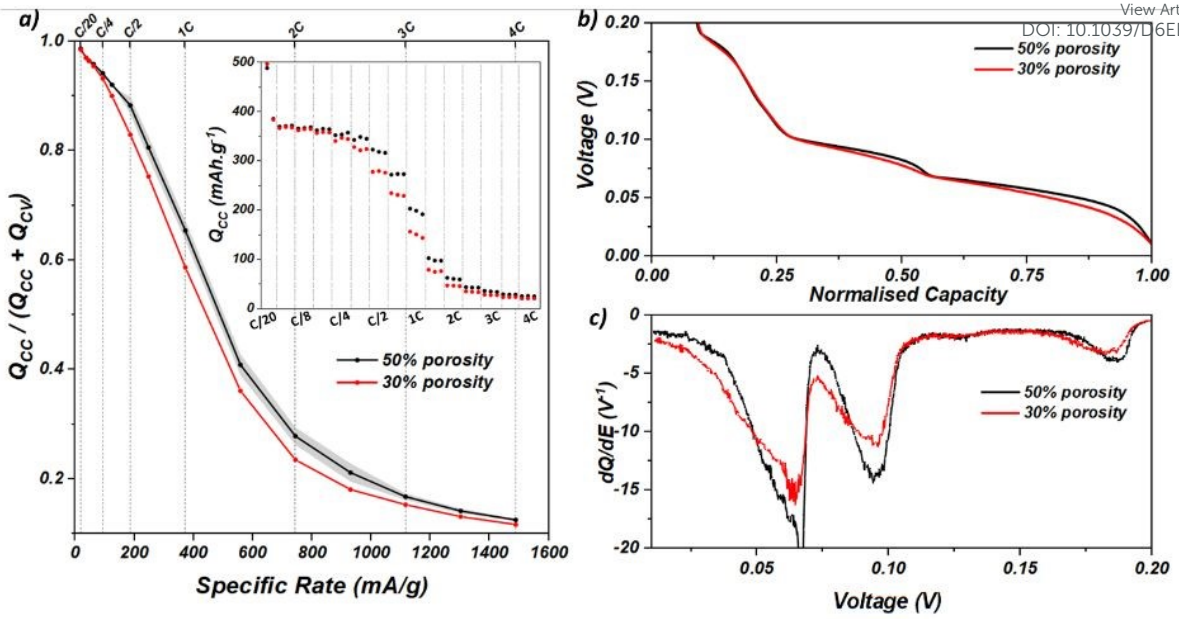

Figure 1: Rate capability test performed on graphite electrodes with 50% and 30% porosity (black and red curves, respectively) cycled vs. Li° in half cells configuration with LP30 electrolyte. a) Proportion of galvanostatic charge (CC) over the total specific capacity obtained by CCCV with a CV period of 30 min, as a function of C-rate applied. Inset represents the specific galvanostatic capacities obtained during the rate capability tests. b) Lithiation profiles obtained at C/4 rate for each electrode porosity. c) Differential Capacity Analysis (DCA) of the lithiation profiles obtained at C/4 rate.

To further characterise the electrochemical behaviour of the two electrode porosities, the lithiation profiles obtained at C/4 are compared (**Figure 1b)**. Regarding the two last potential plateaus (attributed to stage II and stage I formation [35, 36], around 0.8 and 0.05 V), a similar starting potential can be seen; however, the plateau of potential shows a higher tilt for the electrode with 30% porosity. This is even more visible in **Figure 1c**, where the peaks obtained by differential capacity analysis (DCA) are broader and reach lower intensities for the electrode with 30% porosity. All those features highlight higher limitations in the graphite electrode lithiation for 30% porosity, probably linked to electronic and/or ionic transport.

To verify whether the limitation is caused by electronic or ionic percolation, similar rate capability tests were carried out on graphite half cells by changing the salt concentration from 1 M to 0.7 M and 0.35 M $LiPF_6$ in EC/DMC 1:1%$_v$. For all the electrolytes, the first formation cycle was performed at C/20 to ensure a good SEI passivation. As it is well known that the SEI properties are also dependent of the electrolyte and salt concentration[37–39], we compare the first lithiation in Supporting Information (**Note 3**). The potential of formation of the SEI remains the same i.e. 0.8 V despite having a different salt concentration, as well as the "length" of the plateau indicating that the coulomb exchanged are rather similar. It indicates that the SEI properties remain similar in the three cases, even if we cannot exclude a small difference in the chemical properties. **Figure 2a** shows the evolution of the galvanostatic contribution depending on the salt concentration as function of the C-rate. The inset gives the specific galvanostatic capacities for all salt concentrations. Two features are observed: i) the specific galvanostatic capacities are lowered by decreasing the salt concentration from C/10 to 2.5C rate and ii) the decrease of galvanostatic contribution with the increase of the C-rate is faster when decreasing the salt concentration. Again, at a rate of 2.5C and above, lithium metal counter electrode is playing a key role independently from the salt concentration in the electrolyte. In **Figure 2b**, one can notice that decreasing the salt concentration induces a less "marked" curve at C/4, losing the typical potential plateau-shape of graphite staging process. From the DCA curves in **Figure 2c**, two phenomena can be observed: i) the three peaks are shifted toward lower potentials (materialised by the horizontal black

View Article Online
DOI: 10.1039/D6EB00003G

arrows) by decreasing the salt concentration; this is due to the higher overpotentials of lithiation originating from the lower concentrations (inducing higher ohmic drop) and/or the lower kinetic of lithiation; ii) the peaks reach lower intensities (materialised by the vertical black arrows) that highlights a partial loss of the flat potential features, because of a more dispersed process in the electrode volume. The effect of salt concentration supports the hypothesis of an ionic limitation in the electrode. Decreasing the salt concentration is causing higher depletions of lithium ions in some part of the electrode volume, inducing lower specific capacities for a given cycling rate and the loss of the typical potential plateau-shape of graphite lithiation.

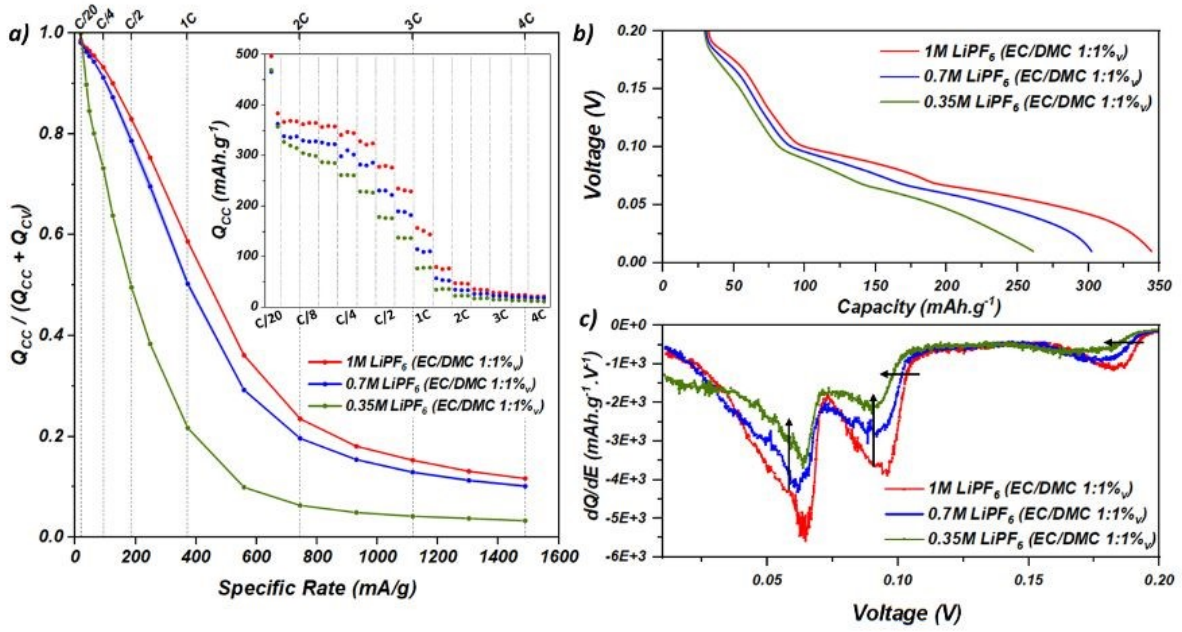

Figure 2: Rate capability test of graphite electrode (30% porosity) cycled vs. Li° in half cells with 1 M, 0.7 M and 0.35 M $LiPF_6$ in EC/DMC 1:1%$_v$ (red, blue and green curves respectively). a) Proportion of galvanostatic charge (CC) over the total specific capacity obtained by CCCV with a CV period of 30 min, as a function of applied C-rate. Inset represents the galvanostatic capacities obtained during the rate capability tests. b) Lithiation profiles obtained at C/4 rate for each salt concentration. c) Differential Capacity Analysis of the lithiation profiles obtained at C/4 rate.

The rate capability tests coupled to salt concentration decrease demonstrate that ionic diffusion of lithium is the limiting factor regarding the power ability of graphite electrodes. These results are in agreement with literature studies demonstrating similar ionic transport limitations in graphite electrodes. A decrease of the electrode porosity is known to increase the tortuosity, which is responsible for higher diffusion times of lithium ions through the electrode microstructure for a given distance. Tortuosity can be measured with two different methods, either by electrochemical impedance spectroscopy (EIS) and/or by X-ray tomography measurements or focused-ion beam scanning electron microscopy (FIB-SEM). The former is simply referred to tortuosity parameters, whereas the second one is generally called geometric tortuosity. The absolute values between them are different, but the trend remains similar. Yet, we measured the ionic tortuosity using EIS (presented in **Note 1**, **Supporting Information**). For an electrode with 50% porosity, a tortuosity of 7 ± 0.2 was obtained while 9.4 ± 0.7 is obtained for an electrode with a porosity of 30%. The values obtained are in the upper range of reported values for graphite electrodes with similar porosities and particle morphologies (from τ = 5 to 10) [40, 20, 41, 42, 43]. Still, the ionic tortuosity difference between the two electrode porosities is significative and it supports a longer diffusion of lithium ions through the electrode thickness for a porosity of 30%.

b. Morphological characterisation

View Article Online
DOI: 10.1039/D6EB00003G

The graphite electrodes with 50% and 30% porosity were also characterised by X-ray holotomography (ID16B, ESRF, Grenoble) to assess the microstructure of the electrodes (**Figure 3a, d**). From the segmented tomographs (methodology is explained in **Note 2, Supporting Information**), each phase (graphite SFG 6L, carbon-binder domain (CBD), and porosity) was characterised in terms of volume fraction and median local thickness. **Table 1** summarises the main results obtained from the X-ray holotomography measurement for each electrode. First, a good agreement can be found between the theoretical (estimated from the components weight and density) and experimental values when it comes to the volume fraction of the different phases, validating the segmentation process. Due to the reached resolution (voxel size of 50 nm), a small fraction of the pores (<100 nm) was possibly not accessible and instead attributed to graphite and/or CBD phases, as observed in the slight underestimation of the porosity volume fraction. It seems that the calendering does not have a huge impact on the CBD domains since they are of similar thicknesses (195 vs. 240 nm), in the range of the experimental resolution. As expected, the pores size decreases when the porosity of the electrode is decreased (from 510 nm to 370 nm). From the porosity phase, the pores intra-connectivity was evaluated and shows proper wettability of the electrode (100% and 97%, for 50% and 30% porosity respectively). Still, the calendering slightly decreases the intra-connectivity, probably because of the closing of some pores. We also analysed the distribution of porosity along the electrode thickness for both porosities in **Note 4 (Supporting Information)**. We noticed that calendering enabled a homogenisation of the porosity along the electrode thickness, whereas at 50% porosity a higher distribution was observed with larger porosity at the separator/electrode interface reaching 60%.

Table 1: Results obtained from the segmentation of the X-ray holotomography experiments for 50% and 30% porosity graphite electrodes.

Electrode	Graphite		CBD		Porosity		CBD median local thickness	Pores median local thickness	Pores intra-connectivity
	$\%V_{theo}$	$\%V_{exp}$	$\%V_{theo}$	$\%V_{exp}$	$\%V_{theo}$	$\%V_{exp}$			
50%	37%	40%	13%	12%	50%	48%	195 nm	510 nm	100%
30%	53%	57%	17%	18%	30%	25%	240 nm	370 nm	97%

The geometric tortuosity was estimated through geodesic/euclidean distances along the through- and in-plane directions (**Figure 3b, e**). The in-plane and through-plane tortuosity are given in **Figure 3c, f** for the two electrode porosities. A close in-plane tortuosity is found for both electrode porosity (1.13 vs. 1.33), whereas the through-plane tortuosity (from where the calendaring is effective) was increased by the calendering step (1.4 vs. 2.0, for 50% and 30% porosity respectively). A thinner distribution is observed for the in-plane direction compared to the through-plane direction. The geodesic distance maps for in-plane and through-plane directions are given in **Note 5** (**Supporting Information**), with values in agreement with the literature[44]. These observations correlate with the flakes-shape of graphite particles, that are naturally oriented with their basal plane parallel to the current collector plane, generating more tortuous pathways in the through-plane direction. The results are also in agreement with the tortuosity estimated *via* EIS, demonstrating the detrimental effect of decreasing the porosity from 50% to 30% by calendering. The estimated values with both techniques are different because the measured tortuosity are not equivalent. Indeed, whereas electrochemically determined tortuosity is sensitive to all the interactions between lithium ions, the counter anion and the porous structure, the geometrical tortuosity does not account for it and is limited to geodesic distances evaluation restricted by the imaging resolution[45].

View Article Online
DOI: 10.1039/D6EB00003G

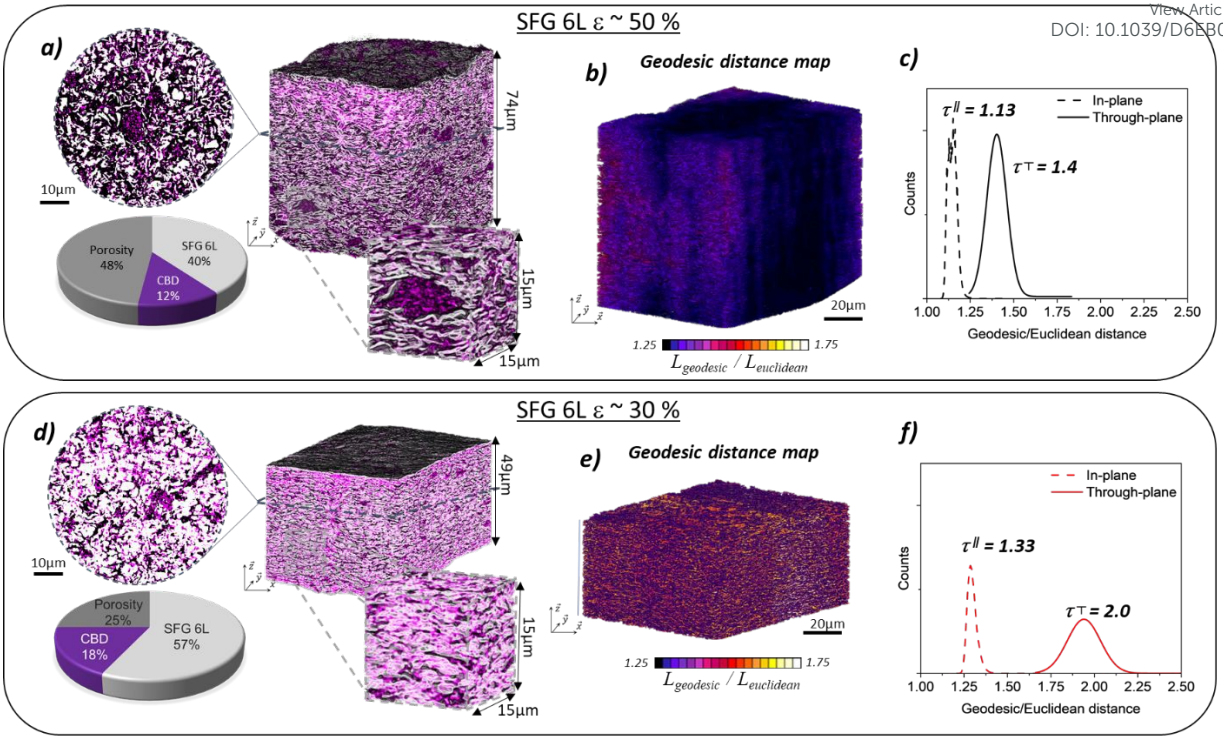

Figure 3: X-ray holotomography results obtained at ID16B beamline at ESRF. a) Segmented image of the 50% porosity graphite electrode, with the volume fraction of each phase. b) Geodesic distance map for the 50% porosity graphite electrode. c) Cumulative geodesic/euclidean distances for the 50% porosity graphite electrode. d) Segmented image of the 30% porosity graphite electrode, with the volume fraction of each phase. e) Geodesic distance map for the 30% porosity graphite electrode. f) Cumulative geodesic/euclidean distances for the 30% porosity graphite electrode.

From these microstructures, diffusion simulations were performed using Cooper's *et al*. software TauFactor[46]. This software was developed to compute effective transport properties in 2D or 3D microstructures by settings specific boundaries condition. Here, the 3D volumes obtained by X-ray holotomography were injected and the effective diffusivity was computed for each electrode porosity. By convention, the methodology imposes the definition of salt concentration boundaries at the separator/electrode and electrode/collector interfaces that were set to C_{sep} = 1 and C_{cc} = 0, since it is commonly accepted that the concentration will be minimal at current collector side. Then, by solving the Laplace equation for steady-states diffusion, the tortuosity factors were computed as described in **Note 2 (Supporting Information)**. This methodology, even though it might seem peculiar, still allows a fair comparison between both electrodes. The simulation results are shown in **Figure 4**, with 3D views of the concentration gradient for both porosities (**Figure 4a, b**). Tortuosity factors of 4.65 for the electrode of 50% porosity, and 17.9 for the electrode of 30% porosity were obtained. The distribution of salt concentration along the electrode thicknesses were also investigated and shown in **Figure 4c**. A linear decrease of the normalised concentration is observed by penetrating the electrode thickness for a porosity of 30%, whereas two slopes (visible with the dashed lines) are observed for the electrode of 50% porosity, with a slope break around 30 µm. This demonstrates a better homogeneity of the electrode's microstructure for a porosity of 30%, due to the higher calendering pressure. Furthermore, the evolution of the median local pore size as a function of the electrode depth is displayed in **Figure 4d**. The profile shows a gradient from larger pore size towards the separator to smaller ones closer to the current collector interface for the poorly-calendered electrode (50% porosity) with variation of more than 10% to the average median local pore thickness value (d_{50} = 510 nm). The same trend is already reported for the local porosity volume fraction as a function of depth in the Supporting Information (**Figure S4a**). On the contrary, a more homogeneous distribution along the electrode

View Article Online
DOI: 10.1039/D0EB00003G

depth is reported for the calendered electrode (i.e. 30% porosity) (less than 3% variation to its average median local pore thickness value of 370 nm). Moreover, the dual-slope behavior observed for the 50% porosity electrode shows an inflexion point that corresponds to the moment when median local pore size goes below the average value of the entire microstructure (at a depth of 33 µm). These observation supports the hypothesis of a more homogenous salt concentration in the more calendered microstructure.

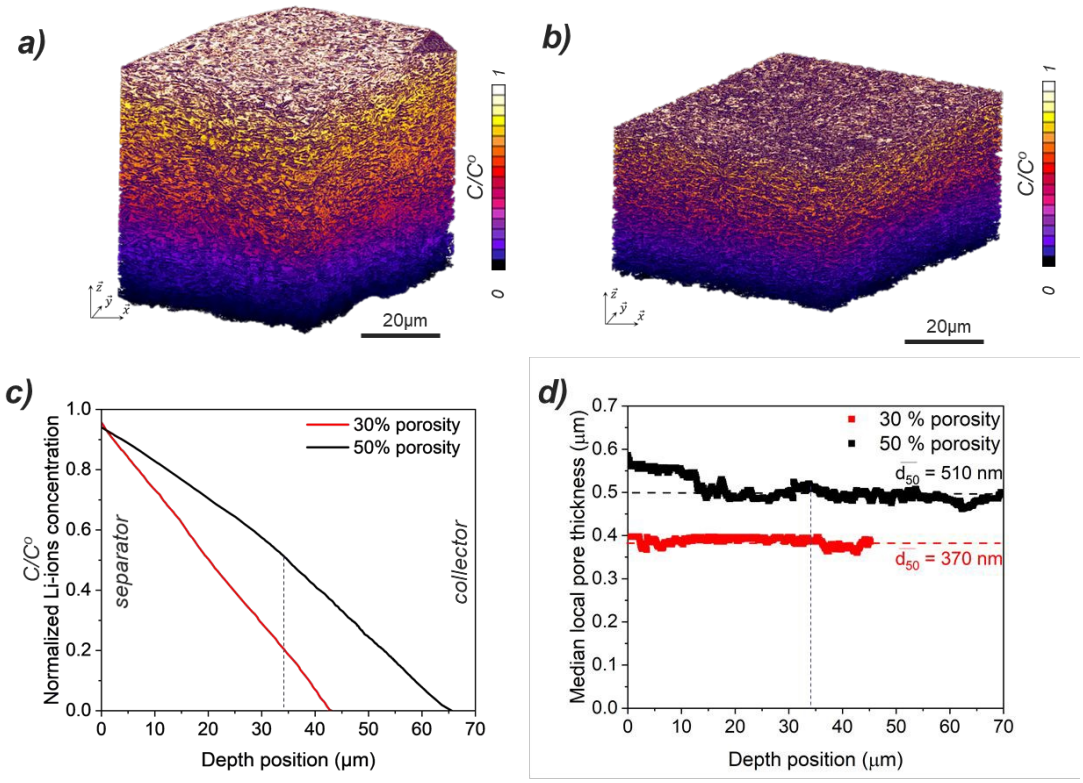

Figure 4: 3D views of the concentration gradient in the electrolyte estimated from the electrode microstructure of a) 50% porosity and b) 30% porosity. c) Normalized concentration profiles along the electrode thicknesses and d) evolution of the median local pore thickness along the electrode depth for both electrodes.

c. *Structural characterisation*

From the preliminary observations obtained by electrochemical and morphological investigations, we expect heterogeneities of lithiation along the electrode thickness, that should be more pronounced for a porosity of 30%. Using the methodology established in this first paper[47], those inhomogeneities were assessed by *z*-profiling experiments using X-ray diffraction at ID31 (ESRF, Grenoble) on the two electrode porosities cycled in half cell vs. Li metal with LP30 electrolyte at 25°C. For sake of clarity, the lag time required for one full *z*-scan is ~ 0.018 h (example of the electrode of 30% porosity) which represents a delta of 0.5% SoC at C/4, 1% SoC at C/2 and 2% SoC at 1C between the position close to the separator and the one close to the current collector, thus it cannot explain the behavior discussed below. In the following, we will discuss the structural state of charge of graphite determined by XRD, assigned to *x* in Li_xC_6. This structural state of charge as to be differentiated from the electrochemical state of charge of the cell (SoC_{cell}), that corresponds to the accumulated amount of charges.

i) ***Structural state of charge determination***

View Article Online
DOI: 10.1039/D6EB00003G

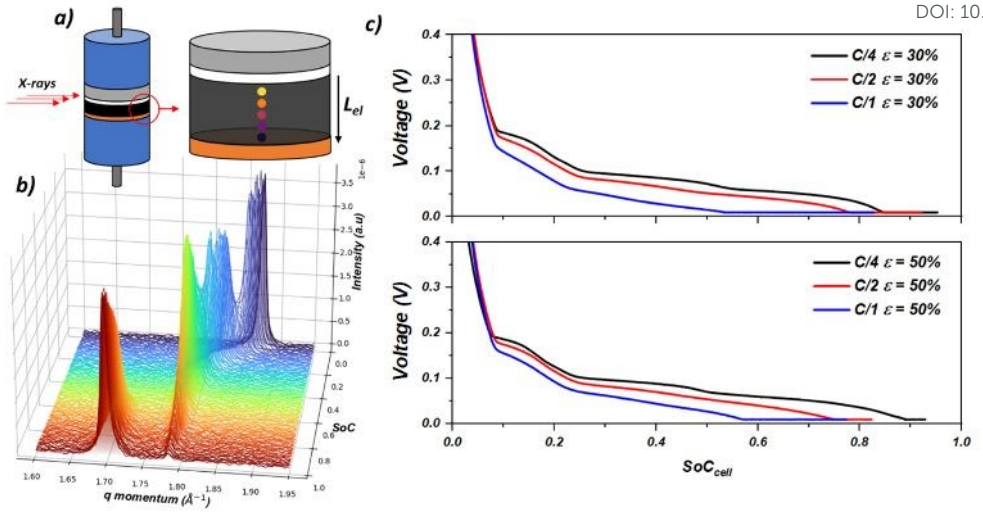

Figure 5: Experimental set-up used at ID31, and main results obtained. a) Scheme of the Swagelok cell probed by X-rays along the thickness of the electrode. b) 3D plot of the diffraction patterns obtained upon lithiation of the 50% porosity electrode at C/4 rate, for the position near the separator (0.1 L). c) Evolution of the cell voltage as a function of the SoC$_{cell}$ for the two electrode porosities, obtained at C/4, C/2 and C/1 rates.

Figure 5 summarises the experiment realised on the lithiation of the graphite half-cells, with the experimental set-up (**Figure 5a**), the X-ray diffractograms obtained during the *operando* measurement at C/4 rate for the porosity of 50%, as an example (**Figure 5b**), and the electrochemical signature obtained at C/4, C/2 and C/1 rate for both porosities (**Figure 5c**). From the diffraction patterns obtained in **Figure 5b**, it was possible to extract the structural state of charge of graphite (x in Li_xC_6) using the methodology developed in this article and the model curve obtained from quasi thermodynamic equilibrium[47]. A summary of the methodology is described in **Note 6** (**Supporting Information**) and the protocol of the z-profiling experiment is given in Material and methods section. The electrochemical signatures of the two cells at C/4 rate are displayed in **Figure 6a, b**, for the 50% and 30% porosities, respectively. The corresponding **Figure 6c, d** show the evolution of the structural state of charge (x in Li_xC_6) for each position in the electrode thickness (from 0.1 L, that is close to the separator, to 0.9 L, close to the current collector) depending on the electrochemical state of charge of the cell (SoC$_{cell}$, determined from integration of current passing through the cell with time). The dispersions of x in Li_xC_6 appear during the potential plateaus for both porosities, with a lithiation front directed from the separator toward the current collector side. This observation leads us to conclude that the limiting process in the power capability of these graphite electrodes is the diffusion of lithium ions through the electrode thickness, since the lithiation front would go in the opposite way in the case of an electronic limitation. Furthermore, graphite possesses a good electronic conductivity and calendaring the electrodes help to gain electronic percolation especially with the usage of conductive agent. However, at very fast charging rate, we cannot exclude that a mixed-control regime could take over.

View Article Online
DOI: 10.1039/D6EB00003G

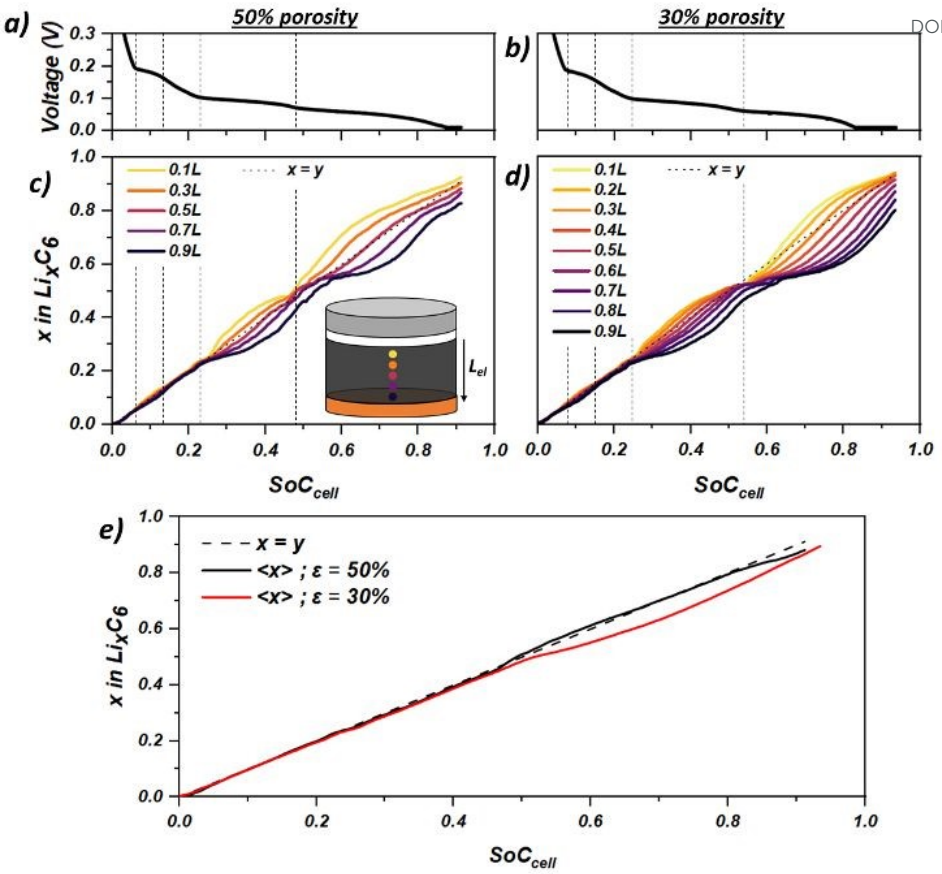

Figure 6: Evolution of structural state of charge (x in Li_xC_6*) for both porosities upon lithiation at C/4 rate. a, b) Graphite potential evolution as a function of cell SoC_{cell}, respectively for 50% and 30% porosity electrodes. c, d) Structural state of charge (x* in Li_xC_6*) evolution as a function of cell SoC_{cell}, respectively for 50% and 30% porosity electrodes. e) Mean structural state of charge (<x>) for both porosities as a function of cell SoC_{cell}.*

Assuming that each electron injected into the graphite conduction band induces the insertion of one lithium ion, a perfect match between the structural state of charge (x in Li_xC_6) and the electrochemical one (SoC_{cell}) should be observed. We compared the evolution of the mean x (<x>) along the electrode thickness with the x = y straight line in **Figure 6e**. One can observe a very good matching between the x = y line and the mean x in Li_xC_6 for the electrode with 50% porosity, even if a slight deviation is noticed around 0.85 SoC_{cell} which correlates with the holding potential period (CV). For the electrode with 30% porosity, a good match is observed from 0 – 0.5 SoC_{cell}; above this value, a deviation reaching maximum 7% appears with the structural state of charge evolving slower than the electrochemical one. To prove that this feature was not generated by the data treatment and is reliable, another method of x in Li_xC_6 determination was applied using the proportions of stage II and stage I phases (see **Note 7, Supporting Information**). A good agreement is obtained between the two methods.

We list several hypotheses to explain the deviation observed for the electrode with 30% porosity:

- Upon cycling, graphite particles undergo volumetric changes reaching + 10% at the end of lithiation [5], translated into a unidirectional expansion increasing the electrode thickness. As a consequence, the z-positions that were probed by the X-ray beam at the beginning of the lithiation are not exactly the same as at the end. Since the electrode thickness expansion is unidirectional and oriented toward the separator, we suppose that the z-positions probed near the current collector do not significantly change upon lithiation, but near the separator the initially probed graphite particles are not anymore in the field of probe as schematised in

View Article Online
DOI: 10.1039/D6EE00003G

Figure 7. With rough calculation for the electrode porosity of 30%, we estimated that the 0.1 L position initially localised 5 µm near the separator should be localised at 12 µm from the separator in the end of lithiation (~0.2 L). Therefore, the volume probed at the end of lithiation might be slightly less representative of the mean structural state of charge (*x* in Li_xC_6), which is a possible explanation for the deviation observed. To justify the difference between the two electrode porosities, we suspect that a large porosity (50%) is more likely to buffer the electrode thickness expansion. Indeed, with a larger fraction of pores, a higher volume is available to accommodate the volume changes, reducing the total thickness expansion upon lithiation. Additionally, the dispersion in structural state of charge (*x* in Li_xC_6) being less important for 50% porosity, this effect is again reduced. To verify this point, we carried out additional experiment using a nano-dilatometer measurement and compared a commercial graphite electrode (around 30% porosity) and a home-made electrode (around 70% porosity). As explained in Supporting Information (**Note 8**), it is difficult to establish a direct correlation between the electrode volume expansion and graphite particle expansion, since microstructural components such as the binder and porosity play significant roles in accommodating volumetric changes. As can be seen in **Figure S11**, nano dilatometric measurements were conducted on a graphite electrode with 70% porosity across several cycles at a very low cycling rate (C/40, determined by the ceramic T-frit separator). The theoretical delithiation of graphite particles (represented by the dotted line) was compared to the measured dilation obtained from the dilatometer. The observed agreement between the dilation profiles was achieved by applying a factor of 0.25 to the theoretical particle dilatation rate, indicating that only one quarter of the particle-level expansion is reflected at the electrode level. This implies that approximately 75% of the particle's expansion is accommodated by electrode porosity and binder deformation. A similar experiment using a commercial electrode demonstrated that when the graphite porosity decreases to 30%, the electrode is capable of buffering only 50% of the volume change[48].

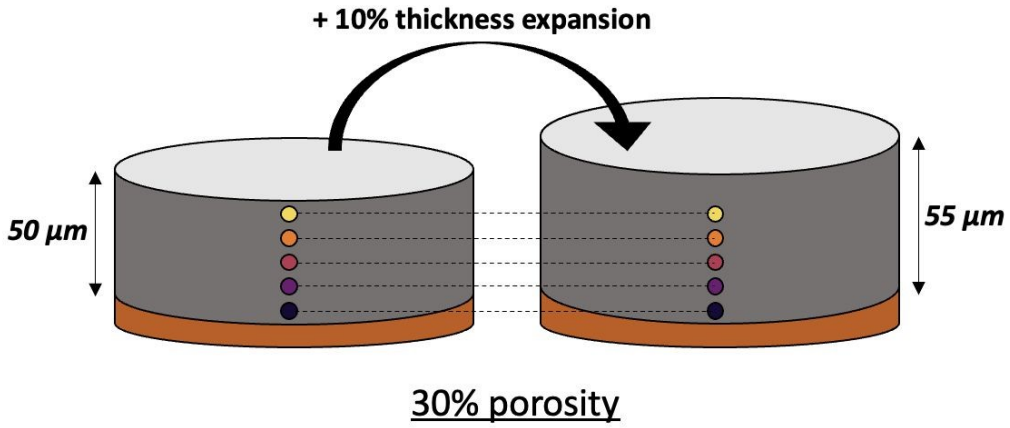

Figure 7: Scheme showing the 30% porosity graphite electrode expansion upon lithiation. The coloured points represent the z-positions probed by the X-ray beam, before and after cycling to show the impact of uniaxial volume changes.

- Another hypothesis relies on the consumption of charges by parasitic reactions such as SEI and/or adsorption. As an example, we suppose that upon lithiation, because of the volume expansion, new "fresh" surfaces of graphite particles are exposed to the electrolyte and solvents reduction can proceed. This would imply the consumption of charges without modifying the structural state of charge, which can contribute to the slight deviation observed.

View Article Online
DOI: 10.1039/D6EB00003G

However, we do not expect a large amount of charges to be consumed by this SEI formation. This solely cannot explain the observed deviation.

ii) Heterogeneities of lithiation

To quantify the heterogeneity of lithiation along the electrode thickness, an Absolute Average Deviation (AAD, **Equation 1**) was calculated by analogy with the NAAD [13, 19].

$$AAD(x) = \frac{1}{L}\int_{z=0}^{z=L} |x(z) - \langle x \rangle_z| \, dz \quad \boldsymbol{Eq.1})$$

with L the electrode thickness, $x(z)$ the structural state of charge at the corresponding *z*-position and $\langle x \rangle_z$ the mean structural state of charge along the electrode thickness. It should be noted that the NAAD parameter has a sensitivity depending on the region of *x* in Li_xC_6, with a higher sensitivity near *x* = 0. On the contrary, the AAD parameter expresses the absolute deviation in *x* in Li_xC_6 with the same sensitivity on the overall lithiation range, bringing the possibility to compare its evolution from *x* = 0 – 1 quantitatively.

Figure 8b plots the evolution of the AAD parameter depending on the SoC_{cell} for the graphite electrode of 50% porosity cycled at C/4 rate. Data are correlated to the graphite electrode potential in **Figure 8a**, and on the right y-axis, to the evolution of d(SoC)/d(E) = f(SoC_{cell}) (this representation is analogue to the DCA analysis, but expressed as a function of the SoC_{cell}). One can observe that low values of AAD are obtained for the regions 1 and 3, involving the transitions of graphite to LiC_{72} (stage I') and LiC_{36} to LiC_{24} (stage IV → stage III), transitions driven by solid solution mechanisms. To contrast, a bell-shaped curve is observed for the AAD parameter in correlation with the peaks observed on the d_{SoC}/d_E representation, note that each peak is linked to a potential plateau ascribed to biphasic mechanisms.

View Article Online
DOI: 10.1039/D6EB00003G

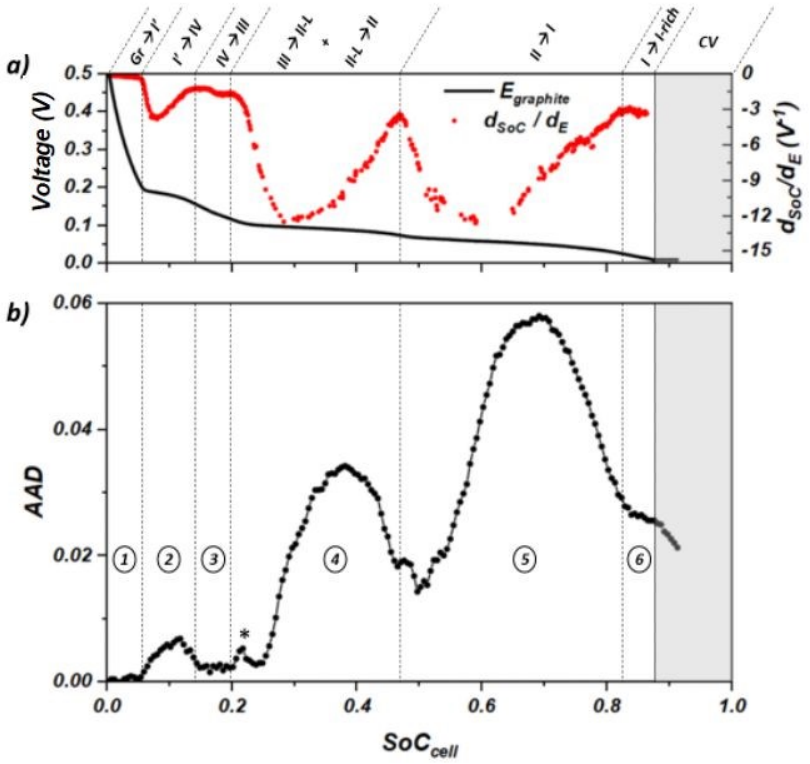

Figure 8: Correlation between the AAD parameter and the electrochemical signature obtained at C/4 rate for the graphite electrode with 50% porosity. a) Evolution of the graphite potential on the left axis and d_{SoC}/d_E on the right axis, as a function of SoC_{cell}. b) Evolution of the AAD parameter as a function of the SoC_{cell}.

The origin of the bell-shaped curve is linked to the nature of lithiation mechanism, here we can take the example of region 2 associated to the stage I' to stage IV transition as described in **Figure 9**:

i) When graphite electrode reaches stage I' (LiC_{72} stoichiometry, **Figure 9a**), no heterogeneity is observed, meaning that graphite enters the first potential plateau of lithiation homogeneously in the electrode volume. Since this transition (stage I' to stage IV) is mainly driven by a biphasic mechanism, the electrochemical potential associated to lithium intercalation is rather constant and homogeneous along the electrode thickness. Then, the consumption rate of lithium ions is controlled only by the local concentration of salt in the electrolyte, which becomes more and more heterogeneous along the electrode thickness upon charging, due to the tortuous microstructure. This is responsible for the generation of salt concentration gradient with depletions in the current collector direction; the consequence is the appearance of heterogeneities of state of charge (increase of the AAD parameter, increasing part of the bell-shaped) with favoured lithiation at the separator/electrode interface.

ii) This biphasic transition ends earlier for graphite particles near the separator side, implying that their electrochemical potential begins to change by entering in the solid solution domain (**Figure 9b**). The latter acts as an activation barrier energy and limits the intercalation of lithium ions. In these conditions, the rate of lithium ions consumption is not only controlled by the salt concentration but also by the electrochemical potential that increases the cost for lithium intercalation. It results in a favourable lithiation of the graphite particles that are still in the biphasic transition, *i.e.* near the current collector side, and a homogenisation of structural state of charge (x in Li_xC_6) is observed (decrease of the AAD parameter leading to the decreasing part of the bell-shaped curve).

View Article Online
DOI: 10.1039/D6EB00003G

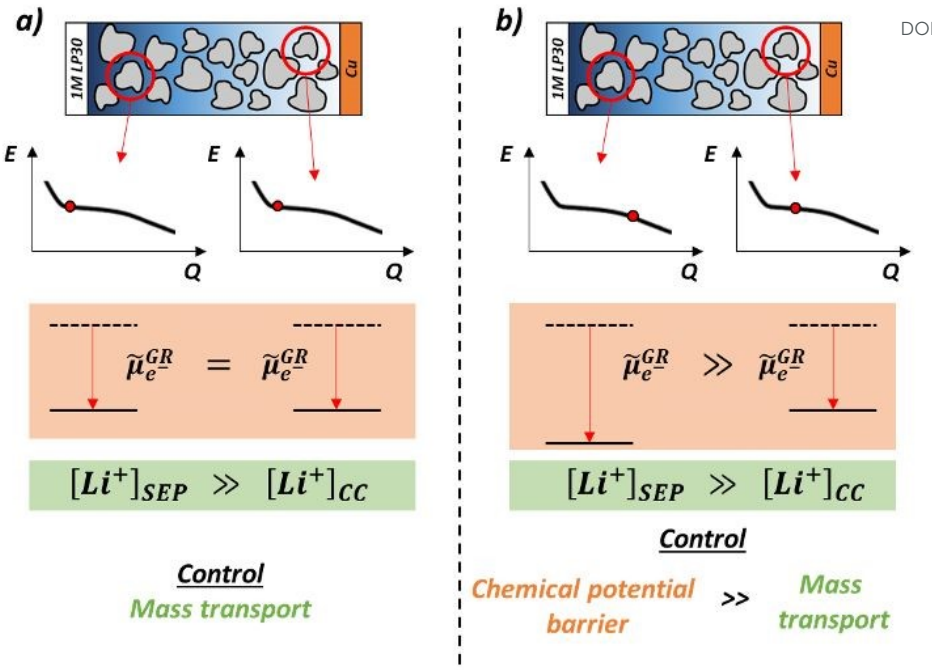

Figure 9: Scheme of the AAD bell-shaped evolution. a) Graphite particles display similar electrochemical potentials ($\tilde{\mu}_{e^-}^{GR}$), meaning that the lithiation is favoured near the separator. b) A chemical potential barrier limits the lithiation near the separator, the lithiation becomes favourable near the current collector. $[Li^+]_{sep}$ and $[Li^+]_{cc}$ correspond to the lithium concentration in the electrode porosity near the separator or near the current collector.

Pursuing our investigation with the region 4, one can notice a slight increase of dispersion in *x* between 0.2 and 0.25 SoC_{cell}, materialised by the asterisk in **Figure 8b**, which can be due to the transition between stage III to stage II-L (LiC_{24} to LiC_{18}) that is partially driven by biphasic mechanism as discussed in a first paper[47]. Entering stage II formation at 0.25 SoC_{cell}, a large increase of dispersion in *x* (second largest bell-shaped) is observed. The larger heterogeneity compared to the first bell-shaped (stage IV formation) is related to the higher number of exchanged coulombs on this second potential plateau. At the end of the stage II formation, the dispersion in *x* did not disappear totally, meaning that the re-homogenisation of state of charge was partial, despite the potential drop between the two-last potential plateaus. Therefore, the dispersion in *x* observed in region 5 during the biphasic transition between stage II to stage I (LiC_{12} to ~$Li_{0.9}C_6$) is even more pronounced. Between 0.83 and 0.88 SoC_{cell} (region 6), a rather stable AAD evolution is noticed and correlates with the transition between stage I and the enriched-stage I, materialised by the stable period on the d_{SoC}/d_E representation. This specific feature is like the trend observed for the transitions involving solid solutions (Gr → stage I' and stage IV → stage III, region 1 and 3 respectively), it supports the existence of solid solutions during the enrichment of stage I to form the LiC_6 phase as discussed previously[47].

The impact of the porosity on the AAD parameter can be seen in **Figure 10a**. A similar evolution of the AAD parameter of the two electrodes with different porosities is noticed until 0.25 SoC_{cell} meaning that the distribution in *x* is similar in both cases, independently of the microstructure of the electrodes. On the contrary, a larger heterogeneity in *x* is observed for the second bell-shaped (associated to stage II formation) for the electrode with the porosity of 30%. The latter is highlighted in **Figure 10b**, where the structural state of charge at the current collector side (0.9 L) is plotted for both porosities. Starting from 0.25 SoC_{cell}, the 0.9 L position for 30% porosity is more delayed in terms of structural state of charge evolution (below the x=y line). This is directly linked to the so-called penetration depth of lithium ions that is lower for this electrode porosity (higher tortuosity), meaning that the kinetics of lithiation at an equivalent relative depth (0.9 L) is lower. Pursuing with the last bell-shaped, the

View Article Online
DOI: 10.1039/D6EB00003G

dispersion in *x* is even larger for 30% porosity. Notice that at the end of the galvanostatic part (materialised by a star on both AAD curves), the electrode with 30% porosity is way more heterogeneous in structural state of charge along its thickness, demonstrating the limitation for power applications.

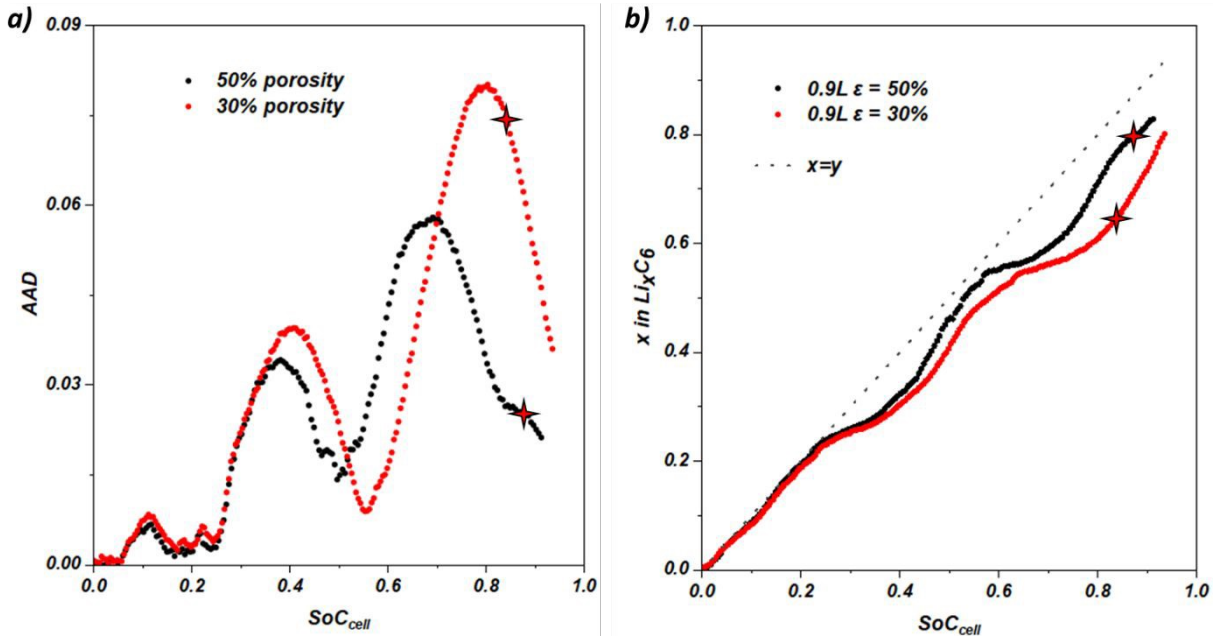

Figure 10: Comparison of the lithiation heterogeneity for the 30% and 50% electrode porosity. a) Evolution of the AAD parameter as a function of the SoC$_{cell}$ for both porosities. b) Evolution of the structural state of charge at 0.9 L for the two electrode porosities depending on the SoC$_{cell}$.

iii) Cycling rate and current distribution

Here, we discuss the rate capability measurement of the 50% porosity graphite electrode in terms of dispersion in *x* (at C/4, C/2 and C/1, **Figure 11a**). For very low SoC$_{cell}$, a similar AAD is observed which is consistent with a cell that is not limited by any transport phenomena. However, pursuing the lithiation, larger heterogeneities are observed by increasing the cycling rate, with higher AAD values at the maxima of the bell-shapes. Additionally, in the regions where the structural state is re-homogenised (such as at SoC$_{cell}$ = 0.5), one can notice the higher AAD values by increasing the C-rate, which reflects the difficulty to homogenise the lithium content along the electrode thickness. The increase in the AAD parameter as a function of the cycling rate is larger for the second bell-shaped (materialised by the black arrow) than the last one (materialised by the red arrow), meaning that the graphite electrode power ability seems to be more C-rate dependent from 0.25 – 0.6 SoC$_{cell}$ than above. The evolution of x in Li$_x$C$_6$ at the 0.9 L position (near the current collector) is plotted in **Figure 11b** as a function of the applied C-rate. By increasing the cycling rate, one can observe a structural state of charge being more and more delayed by deviating from the straight line in the region 0.25 – 0.6 cell SoC$_{cell}$ (this is true for C/4 and C/2 rates that are in CC mode, whereas at C/1 rate the cell entered the CV mode at ~0.55 SoC$_{cell}$). One interesting feature to note is that when the structural state is above *x* = 0.55 (at the potential step between the stage II formation and the stage I formation), no additional delay is observed by increasing the C-rate. This highlights the lower dependence to C-rate increase in

View Article Online
DOI: 10.1039/D6EB00003G

this region of SoC_{cell} (x > 0.55). The data for the electrode with 30% porosity are given in **Note 9** (**Supporting Information**) and present very similar behaviour as for the electrode with 50% porosity.

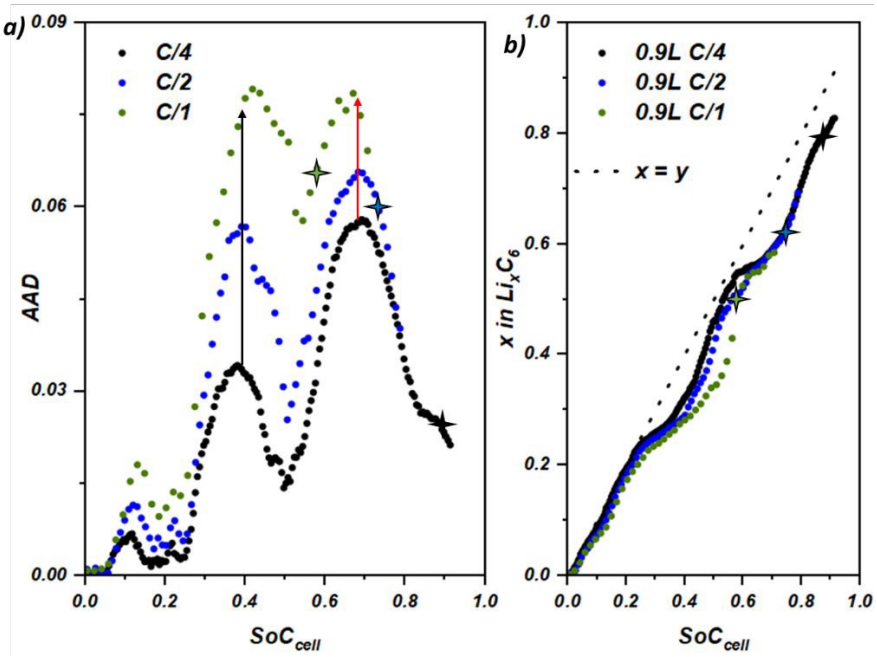

Figure 11: Evolution of structural state of charge dispersion for 50% porosity graphite electrode at different cycling rates. a) Evolution of the AAD parameter as a function of SoC_{cell} for different cycling rates. b) Structural state of charge evolution as a function of the SoC_{cell} at the 0.9 L position (near the current collector) for different cycling rates.

We demonstrated here the detrimental impact of the high ionic tortuosity in the through-plane direction of graphite electrodes with flakes particle-shape, despite having almost 100% of interconnected porosity, meaning no problem of wetting in the electrode depth. The limited penetration depth of lithium ions through the electrode microstructure during fast lithiation generates depletions of salt concentration that appear upon charging, and it implies a current distribution that should be heterogeneous along the electrode thickness. We further analysed the local current distribution for the electrode porosity of 30%. By plotting the differential evolution of *x* in Li_xC_6 as a function of the electrochemical SoC_{cell} for each *z*-position (**Figure 6c, d**), we determined the equivalent current of lithiation (effective C-rate) along the electrode thickness. The effective C-rate corresponds to the rate of structural state of charge evolution for a given scanned position and state of charge as a function of the global cell state of charge. Physically, it is an estimation of the lithiation rate, determined through the structural variations of the graphite particles. However, this is an estimation of the current only responsible for lithium intercalation, and does not consider eventual secondary reactions such as SEI formation. **Figure 12** shows the evolution of effective C-rate for the graphite electrode with 30% porosity, at the *z*-positions 0.1 L (near the separator) and 0.9 L (near the current collector), for the three applied C-rate. All the others position from 0.1 L to 0.9 L recorded at a rate of C/4 is displayed in Note 10 (Figure S13). With this representation, we can easily observe that the distribution of current is favoured near the separator. As an example, looking at **Figure 12a** around 0.1 SoC_{cell}, the 0.1 L position is in higher-regime of lithiation exceeding the applied C-rate (0.25, C/4) while the 0.9 L position displays a lower-regime of lithiation. In contrast, at other times of the cell lithiation (0.5 SoC_{cell} for example), the effective C-rate is higher for the 0.9 L position and the 0.1 L position displays a lower-regime of lithiation. With this, we observe opposite trends for the two curves, and this is in agreement with the behaviour described above. During the two-phase transitions (potential plateaus) the current is distributed where the resistance is the lowest, then near the separator because of a higher local salt concentration. This corresponds to a mass-transport limited period. Once the

View Article Online
DOI: 10.1039/D6EB00003G

graphite particles near the separator exit the potential plateau, an extra resistance appears due to the decrease of the electrochemical potential, which redistributes the current to the delayed regions still in the potential plateau (near the current collector). This corresponds to a period combining mass-transport limitation and an extra potential resistance limitation. This specific trend is repeated along the cell lithiation because of the several plateaus of potential that graphite undergoes, and this explains the opposite trends of effective C-rates near the separator and the current collector observed in **Figure 12**. In addition, we noticed that the maximal effective C-rate reached (between 0.1 L and 0.9 L) is around two times higher than the applied C-rate, regardless of the cycling rate. We observe that the mid-Z-position thickness experiences a lower amplification of effective C-rate (~ 1.5 amplification compared to x2) (Figure S11). The same trend was observed for the graphite electrode with 50% porosity, with similar maximal effective C-rates (**Note 11, Supporting Information**).

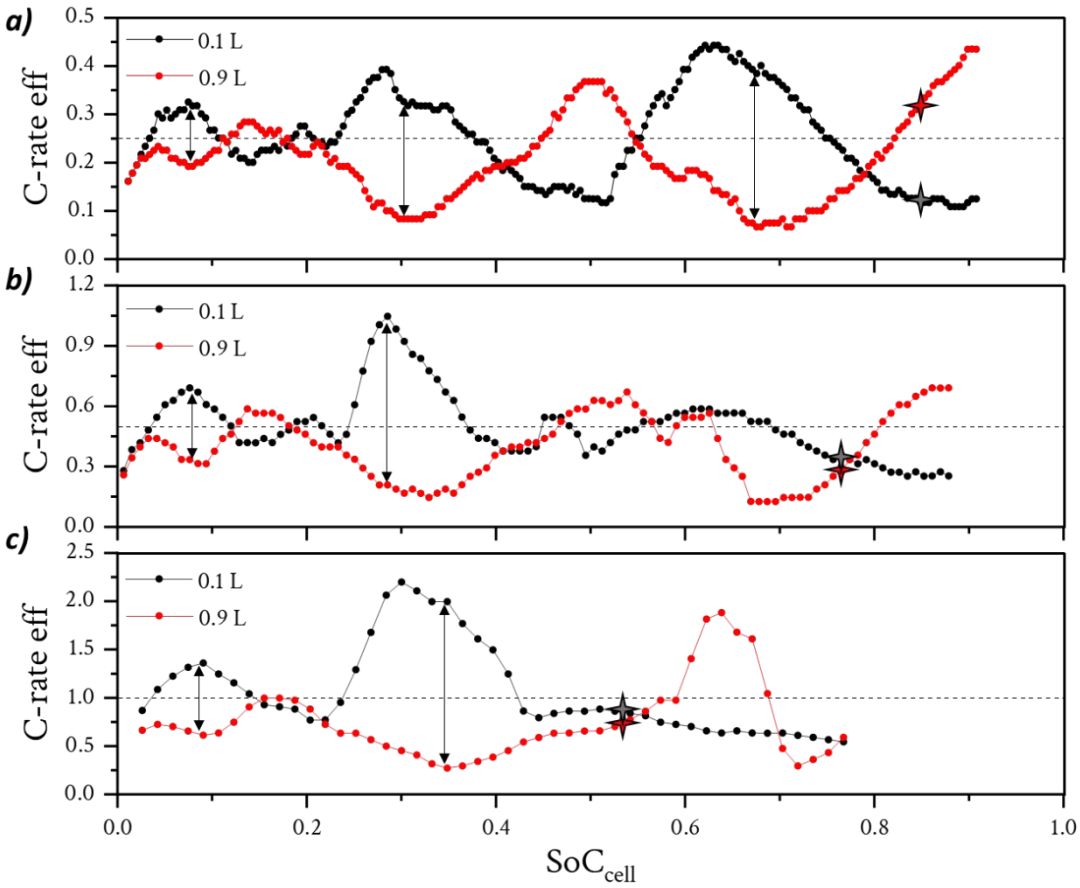

Figure 12: Evolution of effective C-rates as a function of SoC$_{cell}$ at the positions 0.1 L and 0.9 L (black and red curves, respectively) for the graphite electrode with 30% porosity. a) Cycling rate of C/4, the dashed line at 0.25 corresponds to the applied C-rate at the cell level. b) Cycling rate of C/2. c) Cycling rate of C/1. The double arrows highlight the regions where electrons are distributed in priority near the separator/electrode interface. The switch between CC and CV periods is indicated by the red and grey stars.

These current distributions through the electrode thickness raise important questions about aging. We expect higher degradation processes near the separator / electrode interface for at least two reasons: i) graphite particles systematically reach higher SoC and then undergo higher volumetric changes that can be detrimental on long term cycling; ii) higher kinetics of lithiation are observed near the separator, that probably can increase the local temperature and degrade the electrolyte and/or the SEI.

Conclusion

View Article Online
DOI: 10.1039/D6EB00003G

Rate capability tests were performed on graphite electrodes of 50% and 30% porosity, by varying the electrolyte's salt concentration showing high power limitation for electrode with 30% porosity. An in-depth morphological investigation, carried out by X-ray holotomography reveals a high tortuosity pathway for less porous electrode indicating a probable ionic transport limitation. Those results were correlated by operando X-ray diffraction performed in Z-profile of the electrode.

A gradient of lithiation was indeed highlighted from the separator/electrode interface to the current collector/electrode one, validating a power limited by the transport of lithium ions through the electrode microstructures. The analysis of lithiation heterogeneities using AAD revealed a peculiar dynamic depending on the mechanism of lithium insertion. Indeed, it was found that the electrode lithiation was only controlled by mass transport in the biphasic regions, whereas a chemical potential barrier exists during solid solution processes and takes precedence over the mass transport. With the analysis of structural evolution, we estimated the local effective C-rate as a function of the electrode depth. It was observed that local current values can reach two times the applied current, regardless of the electrode porosity.

These works highlight concerns about ageing phenomena for high-rate battery application, because of the local current reaching twice the applied current for a tortuous electrode. These results can serve as experimental data to compare with modelling, based on Newman's model as an example.

Acknowledgement

This work was financed by the Region Auvergne Rhône-Alpes (Pack Ambition Recherche 2021 – Projet IsoBATT) as part of Corentin Renais's thesis. Beamtime at the ESRF was granted within the Battery Pilot Hub MA-4929 "Multi-scale Multi-techniques investigations of Li-ion batteries: towards a European Battery Hub". The authors acknowledge the ID31 beamline (ESRF, Grenoble) and the scientists involved for the XRD experiments (MA-4929 and IH-MA-424). For the morphological analysis, the authors acknowledge the ID16b beamline (ESRF, Grenoble). The following DOI corresponds to the experiment data acquired during these beamtimes: 10.15151/ESRF-ES-1053703088 (MA-4929), 10.15151/ESRF-ES-1397321743 (IH-MA-424) and 10.15151/ESRF-ES-1581887512 (MA-4929).

Declaration of Competing Interest

The authors declare that they have no conflicts of interest to this work.

References

(1) De Rosa, M.; Afanaseva, O.; Fedyukhin, A. V.; Bianco, V. Prospects and Characteristics of Thermal and Electrochemical Energy Storage Systems. *J. Energy Storage* **2021**, *44*, 103443. https://doi.org/10.1016/j.est.2021.103443.

(2) Singh, M.; Kaiser, J.; Hahn, H. Effect of Porosity on the Thick Electrodes for High Energy Density Lithium Ion Batteries for Stationary Applications. *Batteries* **2016**, *2* (4), 35. https://doi.org/10.3390/batteries2040035.

(3) Antartis, D.; Dillon, S.; Chasiotis, I. Effect of Porosity on Electrochemical and Mechanical Properties of Composite Li-Ion Anodes. *J. Compos. Mater.* **2015**, *49* (15), 1849–1862. https://doi.org/10.1177/0021998314568653.

(4) Ji, Y.; Zhang, Y.; Wang, C.-Y. Li-Ion Cell Operation at Low Temperatures. *J. Electrochem. Soc.* **2013**, *160* (4), A636–A649. https://doi.org/10.1149/2.047304jes.

(5) Schweidler, S.; De Biasi, L.; Schiele, A.; Hartmann, P.; Brezesinski, T.; Janek, J. Volume Changes of Graphite Anodes Revisited: A Combined *Operando* X-Ray Diffraction and *In Situ* Pressure Analysis Study. *J. Phys. Chem. C* **2018**, *122* (16), 8829–8835. https://doi.org/10.1021/acs.jpcc.8b01873.

(6) Fongy, C.; Gaillot, A.-C.; Jouanneau, S.; Guyomard, D.; Lestriez, B. Ionic vs Electronic Power Limitations and Analysis of the Fraction of Wired Grains in LiFePO[Sub 4] Composite Electrodes. *J. Electrochem. Soc.* **2010**, *157* (7), A885. https://doi.org/10.1149/1.3432559.

(7) Fongy, C.; Jouanneau, S.; Guyomard, D.; Badot, J. C.; Lestriez, B. Electronic and Ionic Wirings Versus the Insertion Reaction Contributions to the Polarization in LiFePO[Sub 4] Composite Electrodes. *J. Electrochem. Soc.* **2010**, *157* (12), A1347. https://doi.org/10.1149/1.3497353.

(8) Newman, J. S.; Tobias, C. W. Theoretical Analysis of Current Distribution in Porous Electrodes. *J. Electrochem. Soc.* **1962**, *109* (12), 1183. https://doi.org/10.1149/1.2425269.

(9) Doyle, M.; Fuller, T. F.; Newman, J. Modeling of Galvanostatic Charge and Discharge of the Lithium/Polymer/Insertion Cell. *J. Electrochem. Soc.* **1993**, *140* (6), 1526–1533. https://doi.org/10.1149/1.2221597.

(10) Fuller, T. F.; Doyle, M.; Newman, J. Simulation and Optimization of the Dual Lithium Ion Insertion Cell. *J. Electrochem. Soc.* **1994**, *141* (1), 1–10. https://doi.org/10.1149/1.2054684.

(11) Gallagher, K. G.; Trask, S. E.; Bauer, C.; Woehrle, T.; Lux, S. F.; Tschech, M.; Lamp, P.; Polzin, B. J.; Ha, S.; Long, B.; Wu, Q.; Lu, W.; Dees, D. W.; Jansen, A. N. Optimizing Areal Capacities through Understanding the Limitations of Lithium-Ion Electrodes. *J. Electrochem. Soc.* **2016**, *163* (2), A138–A149. https://doi.org/10.1149/2.0321602jes.

(12) Tambio, S. J.; Cadiou, F.; Maire, E.; Besnard, N.; Deschamps, M.; Lestriez, B. The Concept of Effective Porosity in the Discharge Rate Performance of High-Density Positive Electrodes for Automotive Application. *J. Electrochem. Soc.* **2020**, *167* (16), 160509. https://doi.org/10.1149/1945-7111/abcb42.

(13) Dufour, N.; Chandesris, M.; Geniès, S.; Cugnet, M.; Bultel, Y. Lithiation Heterogeneities of Graphite According to C-Rate and Mass-Loading: A Model Study. *Electrochimica Acta* **2018**, *272*, 97–107. https://doi.org/10.1016/j.electacta.2018.03.196.

(14) Gu, H. Mathematical Analysis of a Zn / NiOOH Cell. *J. Electrochem. Soc.* **1983**, *130* (7), 1459–1464. https://doi.org/10.1149/1.2120009.

(15) Dawkins, J. I. G.; Martens, I.; Danis, A.; Beaulieu, I.; Chhin, D.; Mirolo, M.; Drnec, J.; Schougaard, S. B.; Mauzeroll, J. Mapping the Total Lithium Inventory of Li-Ion Batteries. *Joule* **2023**, *7* (12), 2783–2797. https://doi.org/10.1016/j.joule.2023.11.003.

(16) Hogrefe, C.; Waldmann, T.; Molinero, M. B.; Wildner, L.; Axmann, P.; Wohlfahrt-Mehrens, M. Cross-Sectional In Situ Optical Microscopy with Simultaneous Electrochemical Measurements for Lithium-Ion Full Cells. *J. Electrochem. Soc.* **2022**, *169* (5), 050519. https://doi.org/10.1149/1945-7111/ac6c57.

(17) Kang, S.; Yeom, S. J.; Lee, H. Side-View Operando Optical Microscopy Analysis of a Graphite Anode to Study Its Kinetic Hysteresis. *ChemSusChem* **2020**, *13* (6), 1480–1484. https://doi.org/10.1002/cssc.201903289.

(18) Yao, K. P. C.; Okasinski, J. S.; Kalaga, K.; Shkrob, I. A.; Abraham, D. P. Quantifying Lithium Concentration Gradients in the Graphite Electrode of Li-Ion Cells Using *Operando* Energy Dispersive X-Ray Diffraction. *Energy Environ. Sci.* **2019**, *12* (2), 656–665. https://doi.org/10.1039/C8EE02373E.

(19) Tardif, S.; Dufour, N.; Colin, J.-F.; Gébel, G.; Burghammer, M.; Johannes, A.; Lyonnard, S.; Chandesris, M. Combining *Operando* X-Ray Experiments and Modelling to Understand the Heterogeneous Lithiation of Graphite Electrodes. *J. Mater. Chem. A* **2021**, *9* (7), 4281–4290. https://doi.org/10.1039/D0TA10735B.

(20) Landesfeind, J.; Hattendorff, J.; Ehrl, A.; Wall, W. A.; Gasteiger, H. A. Tortuosity Determination of Battery Electrodes and Separators by Impedance Spectroscopy. *J. Electrochem. Soc.* **2016**, *163* (7), A1373–A1387. https://doi.org/10.1149/2.1141607jes.

(21) Martínez-Criado, G.; Villanova, J.; Tucoulou, R.; Salomon, D.; Suuronen, J.-P.; Labouré, S.; Guilloud, C.; Valls, V.; Barrett, R.; Gagliardini, E.; Dabin, Y.; Baker, R.; Bohic, S.; Cohen, C.; Morse, J. ID16B: A

Hard X-Ray Nanoprobe Beamline at the ESRF for Nano-Analysis. *J. Synchrotron Radiat.* **2016**, *23* (1), 344–352. https://doi.org/10.1107/S1600577515019839.

(22) Cloetens, P.; Ludwig, W.; Baruchel, J.; Van Dyck, D.; Van Landuyt, J.; Guigay, J. P.; Schlenker, M. Holotomography: Quantitative Phase Tomography with Micrometer Resolution Using Hard Synchrotron Radiation x Rays. *Appl. Phys. Lett.* **1999**, *75* (19), 2912–2914. https://doi.org/10.1063/1.125225.

(23) Mirone, A.; Brun, E.; Gouillart, E.; Tafforeau, P.; Kieffer, J. The PyHST2 Hybrid Distributed Code for High Speed Tomographic Reconstruction with Iterative Reconstruction and a Priori Knowledge Capabilities. *Nucl. Instrum. Methods Phys. Res. Sect. B Beam Interact. Mater. At.* **2014**, *324*, 41–48. https://doi.org/10.1016/j.nimb.2013.09.030.

(24) Lyckegaard, A.; Johnson, G.; Tafforeau, P. Correction of Ring Artifacts in X-Ray Tomographic Images. *Int. J. Tomogr. Stat.* **2011**, *18* (1–9).

(25) Schindelin, J.; Arganda-Carreras, I.; Frise, E.; Kaynig, V.; Longair, M.; Pietzsch, T.; Preibisch, S.; Rueden, C.; Saalfeld, S.; Schmid, B.; Tinevez, J.-Y.; White, D. J.; Hartenstein, V.; Eliceiri, K.; Tomancak, P.; Cardona, A. Fiji: An Open-Source Platform for Biological-Image Analysis. *Nat. Methods* **2012**, *9* (7), 676–682. https://doi.org/10.1038/nmeth.2019.

(26) Berg, S.; Kutra, D.; Kroeger, T.; Straehle, C. N.; Kausler, B. X.; Haubold, C.; Schiegg, M.; Ales, J.; Beier, T.; Rudy, M.; Eren, K.; Cervantes, J. I.; Xu, B.; Beuttenmueller, F.; Wolny, A.; Zhang, C.; Koethe, U.; Hamprecht, F. A.; Kreshuk, A. Ilastik: Interactive Machine Learning for (Bio)Image Analysis. *Nat. Methods* **2019**, *16* (12), 1226–1232. https://doi.org/10.1038/s41592-019-0582-9.

(27) Kieffer, J.; Wright, J. P. PyFAI: A Python Library for High Performance Azimuthal Integration on GPU. *Powder Diffr.* **2013**, *28* (S2), S339–S350. https://doi.org/10.1017/S0885715613000924.

(28) The Matplotlib Development Team. Matplotlib: Visualization with Python, 2024. https://doi.org/10.5281/ZENODO.592536.

(29) Newville, M.; Stensitzki, T.; Allen, D. B.; Ingargiola, A. LMFIT: Non-Linear Least-Square Minimization and Curve-Fitting for Python, 2014. https://doi.org/10.5281/ZENODO.11813.

(30) Erb, D. Pybaselines: A Python Library of Algorithms for the Baseline Correction of Experimental Data, 2024. https://doi.org/10.5281/ZENODO.5608581.

(31) Heubner, C.; Lämmel, C.; Nickol, A.; Liebmann, T.; Schneider, M.; Michaelis, A. Comparison of Chronoamperometric Response and Rate-Performance of Porous Insertion Electrodes: Towards an Accelerated Rate Capability Test. *J. Power Sources* **2018**, *397*, 11–15. https://doi.org/10.1016/j.jpowsour.2018.06.087.

(32) Sivakkumar, S. R.; Nerkar, J. Y.; Pandolfo, A. G. Rate Capability of Graphite Materials as Negative Electrodes in Lithium-Ion Capacitors. *Electrochimica Acta* **2010**, *55* (9), 3330–3335. https://doi.org/10.1016/j.electacta.2010.01.059.

(33) Buqa, H.; Goers, D.; Holzapfel, M.; Spahr, M. E.; Novák, P. High Rate Capability of Graphite Negative Electrodes for Lithium-Ion Batteries. *J. Electrochem. Soc.* **2005**, *152* (2), A474. https://doi.org/10.1149/1.1851055.

(34) Lu, D.; Shao, Y.; Lozano, T.; Bennett, W. D.; Graff, G. L.; Polzin, B.; Zhang, J.; Engelhard, M. H.; Saenz, N. T.; Henderson, W. A.; Bhattacharya, P.; Liu, J.; Xiao, J. Failure Mechanism for Fast-Charged Lithium Metal Batteries with Liquid Electrolytes. *Adv. Energy Mater.* **2015**, *5* (3), 1400993. https://doi.org/10.1002/aenm.201400993.

(35) Fujimoto, H.; Yamaki, T.; Shimoda, K.; Fujinami, S.; Nakatani, T.; Kano, G.; Kawasaki, M.; Ogumi, Z.; Abe, T. Phase Diagram of Li-Graphite Intercalation Compound Formed by the Charge/Discharge Reaction in Li-Ion Battery. *J. Electrochem. Soc.* **2022**, *169* (7), 070507. https://doi.org/10.1149/1945-7111/ac7e77.

(36) Takagi, S.; Shimoda, K.; Haruyama, J.; Kiuchi, H.; Okazaki, K.; Fukunaga, T.; Ogumi, Z.; Abe, T. Operando Structural Analysis of Phase Transition of Graphite Electrode during Li De-Intercalation Process Using Neutron and Synchrotron Radiation X-Ray Diffraction. *Carbon* **2023**, *215*, 118414. https://doi.org/10.1016/j.carbon.2023.118414.

(37) Camacho-Forero, L. E.; Smith, T. W.; Balbuena, P. B. Effects of High and Low Salt Concentration in Electrolytes at Lithium–Metal Anode Surfaces. *J. Phys. Chem. C* **2017**, *121* (1), 182–194. https://doi.org/10.1021/acs.jpcc.6b10774.

(38) Nie, M.; Lucht, B. L. Role of Lithium Salt on Solid Electrolyte Interface (SEI) Formation and Structure in Lithium Ion Batteries. *J. Electrochem. Soc.* **2014**, *161* (6), A1001–A1006. https://doi.org/10.1149/2.054406jes.

(39) Hao, M.; Weng, S.; Zhong, C.; Li, Y.; Wang, X. Structure and Evolution of Solid Electrolyte Interphase (SEI) at the Electrode-Electrolyte Interface. *Mater. Today Energy* **2025**, *53*, 101998. https://doi.org/10.1016/j.mtener.2025.101998.

(40) Malifarge, S.; Delobel, B.; Delacourt, C. Determination of Tortuosity Using Impedance Spectra Analysis of Symmetric Cell. *J. Electrochem. Soc.* **2017**, *164* (11), E3329–E3334. https://doi.org/10.1149/2.0331711jes.

(41) Landesfeind, J.; Ebner, M.; Eldiven, A.; Wood, V.; Gasteiger, H. A. Tortuosity of Battery Electrodes: Validation of Impedance-Derived Values and Critical Comparison with 3D Tomography. *J. Electrochem. Soc.* **2018**, *165* (3), A469–A476. https://doi.org/10.1149/2.0231803jes.

(42) Zacharias, N. A.; Nevers, D. R.; Skelton, C.; Knackstedt, K.; Stephenson, D. E.; Wheeler, D. R. Direct Measurements of Effective Ionic Transport in Porous Li-Ion Electrodes. *J. Electrochem. Soc.* **2013**, *160* (2), A306–A311. https://doi.org/10.1149/2.062302jes.

(43) Guo, Y.; Li, X.; Qin, Q.; Wang, Z.; Guo, H.; Wang, J.; Yan, G. Determination of the Tortuosity and Contact Resistances in Thick Graphite Anodes via Electrochemical Impedance Spectroscopy. *J. Power Sources* **2023**, *569*, 233003. https://doi.org/10.1016/j.jpowsour.2023.233003.

(44) Kroll, M.; Hlushkou, D.; Schlabach, S.; Höltzel, A.; Roling, B.; Tallarek, U. Reconstruction–Simulation Approach Verifies Impedance-Derived Ion Transport Tortuosity of a Graphite Battery Electrode. *J. Electrochem. Soc.* **2018**, *165* (13), A3156–A3163. https://doi.org/10.1149/2.0711813jes.

(45) Tjaden, B.; Finegan, D. P.; Lane, J.; Brett, D. J. L.; Shearing, P. R. Contradictory Concepts in Tortuosity Determination in Porous Media in Electrochemical Devices. *Chem. Eng. Sci.* **2017**, *166*, 235–245. https://doi.org/10.1016/j.ces.2017.03.051.

(46) Cooper, S. J.; Bertei, A.; Shearing, P. R.; Kilner, J. A.; Brandon, N. P. TauFactor: An Open-Source Application for Calculating Tortuosity Factors from Tomographic Data. *SoftwareX* **2016**, *5*, 203–210. https://doi.org/10.1016/j.softx.2016.09.002.

(47) Renais, C.; Mirolo, M.; Servajon, M.; Drnec, J.; Alloin, F.; Villevieille, C. Understanding Fast Charging Ability Limitation in Graphite Electrode for Li-Ion Batteries: Quasi-Thermodynamic Approach and Methodology. *Chem. Mater.* **2025**. https://doi.org/10.1021/acs.chemmater.5c00722.

(48) Renais, C.; Mercier-Guyon, B.; Wasylowski, D.; Sonnet, M.; Dechent, P.; Servajon, M.; Blanc, N.; Lyonnard, S.; Sauer, D. U.; Villevieille, C. Exploring Electrochemical Dynamics in graphite||LiNi0.8Mn0.1Co0.1O2 Cells via Operando Ultrasound and Multiprobe Approaches. *Nat. Commun.* **2025**, *16* (1), 7774. https://doi.org/10.1038/s41467-025-62935-z.

View Article Online
DOI: 10.1039/D6EB00003G

Data availability

Data are available upon reasonable request. DOI for large scale facilities measurements are indictaed as a reference in the manuscropt